PHYSICAL REVIEW B **113**, 205117 (2026)

Dynamics of fractional quantum Hall liquids with a pulse at the edge

Jie Li,[1,2] Chen-Xin Jiang,[1,3] and Zi-Xiang Hu[1,*]
[1]*Department of Physics and Chongqing Key Laboratory for Strongly Coupled Physics, Chongqing University, Chongqing 401331, People's Republic of China*
[2]*College of General Education, Chongqing Polytechnic University of Electronic Technology, Chongqing 401331, People's Republic of China*
[3]*Division of Physics and Applied Physics, Nanyang Technological University, 637371 Singapore*

(Received 18 July 2025; revised 11 April 2026; accepted 21 April 2026; published 6 May 2026)

Motivated by recent experimental advancements in scanning optical stroboscopic confocal microscopy and spectroscopy measurements, which have facilitated exceptional energy-space-time resolution for investigating edge and bulk dynamics in fractional quantum Hall systems, we formulated a model for the pump-probe process on the edge. Starting with a ground state, we applied a tip potential near the fractional quantum Hall liquid edge, which was subsequently turned off after a defined time duration. By examining how the specific nature of the tip potential influences the evolution of the wave function and its distribution in energy spectrum, we identify that quench dynamics of the edge pulse leads to excitations that spread both along the edge and perpendicularly into the bulk. Moreover, magnetoroton excitations are predominant among the bulk excitations. These results align well with the experimental observations. Furthermore, we analyzed the effects of the tip's position, intensity, and duration on the dynamics.

DOI: 10.1103/1h9l-mrdv

I. INTRODUCTION

The fractional quantum Hall effect (FQH), distinguished by topologically protected gapped bulk states and gapless chiral edge states, has become an important framework for investigating novel quantum phenomena within strongly correlated topological systems [1,2]. This contrasts with its integer counterpart, which features as noninteracting state. Due to the exotic properties of the FQH phase, such as fractional charge, fractional statistics, and topological order, its potential applications in areas such as topological quantum computing have attracted widespread attention [3–7]. The FQH state is characterized by compressible metallic edge states and a bulk that is incompressible and insulating. Since the magnetic field breaks time-reversal symmetry, edge modes propagate in only one direction, and conduction is limited to the edges, which can theoretically be described by chiral Luttinger liquid [8,9]. In contrast to the edges, the bulk of the FQH liquid is topologically protected, which is immune to any local perturbation. Thus the excitation in the bulk is also gapped. Girvin *et al.* introduced the single-mode approximation (SMA) to describe the low-energy excitations in the bulk, which are neutral magneto-roton excitations [10–12]. Detecting neutral excitation experimentally poses significant challenges. The bulk-edge correspondence implies that edge modes are typically vital for examining the topological properties of FQH liquids. [13–31].

Excitations at the edge are also known as edge magnetoplasmons (EMPs) or charge density waves, where voltage pulses applied at the edge of a Hall liquid are converted into EMP wave packets and transmitted along the edge adjacent to the injection pulse [32–36]. In general, edge excitations dominate the system's low-energy behavior and possess rich physics, such as anyon statistics [3,15–19], edge reconstruction [20–25], edge tunneling [26–30], and charge-neutral upstream Majorana modes of edge currents [31]. Due to chiral edge modes with edge velocity [37], the properties of edge states are typically measured using shot noise [25,31,38], and thermal transport [39–42], which are basically static measurements. Recent experimental advances in scanning optical stroboscopic confocal microscopy and spectroscopy [43–46] have enabled unprecedented energy-space-time resolution to probe edge and bulk dynamics in FQH systems. For example, pump probe reflectance measurements with ~1 ps temporal resolution revealed distinct EMP modes and nonlinear excitations propagating at velocities of $\sim10^4$–10^5 m/s at $\nu = 1/3$, while time-resolved photoluminescence (PL) spectroscopy highlighted the role of trion lifetimes in limiting temporal resolution (100–300 ps) for edge-state imaging. These studies demonstrated that voltage pulses applied to gate electrodes can generate chiral EMPs whose propagation dynamics reflect the Tomonaga-Luttinger liquid behavior of edge channels. Complementary experiments using spatially resolved PL microscopy visualized bulk magnetoroton excitations (10^3–10^4 m/s) and strain pulses, highlighting the interaction between edge and bulk collective modes in the $\nu = 2/3$ FQH regime [45,46]. Notably, perturbations near the edge, such as gate-induced charge density modulations, were shown to excite both chiral edge waves and bulk modes, with the latter exhibiting velocity dependencies tied to the dielectric environment and Landau-level mixing. However, the microscopic mechanisms that govern the response of the edge to localized potentials, such as tip-induced confinement or disorder [47–51], remain poorly understood. Numerical studies of edge dynamics under tailored tip potentials could bridge this gap,

---

[*] Contact author: zxhu@cqu.edu.cn

offering insights into edge reconstruction, nonlinear excitations, and emergent spacetime metrics predicted in quantum gravity analogs. By validating experimental observations and extending them to atomistic or field-theoretic models, such simulations may elucidate how localized perturbations modify edge-state coherence, fractional statistics, and energy transport, which are critical for advancing FQH-based quantum technologies and fundamental physics.

In this work, we numerically investigate the quench dynamics of a $\nu = 1/3$ Laughlin state under a time-limited tip potential at the edge. By solving the time-dependent Schrödinger equation for a disk geometry with tunable pulse parameters (position w, duration τ, and strength U_δ), we demonstrate that localized perturbations induce (i) chiral edge currents, (ii) bulk diffusion mediated by magnetoroton excitations, and (iii) oscillations in quantum fidelity governed by energy gaps in the rotor spectrum. Our simulations reveal that pulse positioning near electron density maxima enhances bulk-state hybridization, while pulse duration and strength modulate excitation amplitudes through interference effects. These results establish a framework for engineering edge-bulk coupling in FQH systems and provide insights into nonlinear dynamics predicted for quantum spacetime analogs. The remainder of this paper is organized as follows. In Sec. II, we introduce the microscopic model used in this work and describe how to simulate voltage pulses with a tip potential. In Sec. III, we discuss the quench dynamics of the edge within the model Hamiltonian. In Sec. IV, we analyze in detail the factors that affect edge dynamics, including the position, duration, and intensity of the pulse at the edge. Summaries and discussion are given in Sec. V.

II. MICROSCOPIC MODEL

In this work, we consider a two-dimensional electron gas (2DES) system in disk geometry that features an open boundary with a perpendicular magnetic field. The conservation of angular momentum arises from the rotational symmetry, leading to the following single-particle wave function at the lowest Landau level (LLL):

$$|m\rangle = \frac{1}{\sqrt{2\pi} l_B} \frac{1}{\sqrt{2^m m!}} z^m e^{-|z|^2/4l_B^2}, \tag{1}$$

where $z = x + iy$ are the coordinates of the electron in the plane, $l_B = \sqrt{\hbar c/eB}$ is the magnetic length, and m is the angular momentum along the z-axis labels the degenerate orbital states in each Landau level. For a finite system with orbitals N_{orb}, m takes a value from zero to $N_{\text{orb}} - 1$.

As depicted in Fig. 1, a δ potential with strength U_δ at the position w near the boundary mimics the tip potential used in the experiment.

$$V(z) = U_\delta \delta(z - w). \tag{2}$$

While w resides in the bulk, this potential might generate a quasihole excitation [47] with a fractional charge. In the Hilbert space defined by orbitals $\{|m\rangle\}$, the LLL projected matrix element $V_{mn} = \langle m|V(z)|n\rangle$ can be expressed as a one-dimensional integral

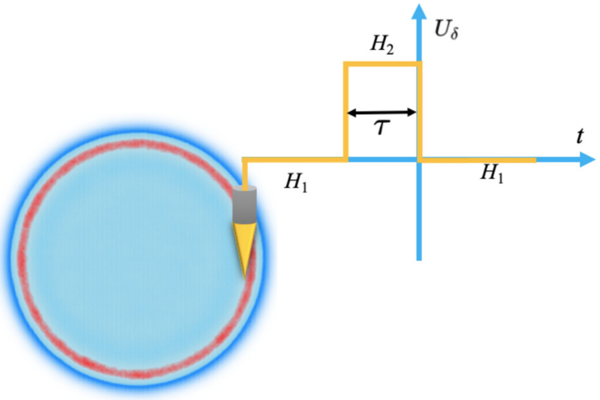

FIG. 1. A tip potential is applied at the edge of a FQH liquid to simulate effect of a voltage pulse. For N_e electrons on a disk, the radius R is $\sqrt{2N_{\text{orb}}}$, and the number of orbitals N_{orb} is $\frac{N_e}{\nu}$. The time evolution process can be divided into three parts: Initially, the system is in the ground state of Hamiltonian H_1. Subsequently, a potential $V(z)$ is applied at the edge of the system for a duration τ (unit: $\hbar\varepsilon l_B/e^2$) to simulate the square voltage pulse as in Ref. [44]. Finally, the moment when the potential is removed is denoted as $t = 0$, and the Hamiltonian reverts to H_1.

$$V_{mn} = \frac{U_\delta}{2^{(n-m)/2}} \sqrt{\frac{m!}{n!}} \int_0^\infty dk e^{-\frac{k^2}{2}} k^{n-m+1} L_m^{n-m}\left(\frac{k^2}{2}\right) \times J_{n-m}(k|w|)\left(\frac{w}{|w|}\right)^{m-n}, \tag{3}$$

with $L_m^k(k)$ representing the generalized Laguerre polynomial and $J_m(k)$ denoting the Bessel function. The Hamiltonian of the system is

$$H_2 = H_1 + V(z)\Theta(t), \tag{4}$$

where $\Theta(t)$ denotes the step function, one for $t \in [0, \tau]$ and 0 otherwise. The second term mimics the tip pulse potential at location w, characterized by a duration τ and an intensity U_δ. The first term H_1, represents the Hamiltonian for electron-electron interactions that hosts the FQH state as the ground state at specific filling. Here, for simplicity, we consider the Laughlin state [2], denoted as $|\Psi_1\rangle$, at $\nu = 1/3$, which is the densest zero-energy eigenstate of the short-range hard-core interaction. In Haldane's pseudopotential formalism [52], this interaction can be described by $V_m = \delta_{1,m}$. Beginning with Ψ_1, applying the tip potential over the time interval τ leads to the state evolving into

$$|\Psi(0)\rangle = \exp(-iH_2\tau/\hbar)|\Psi_1\rangle. \tag{5}$$

We label this as the initial state at $t = 0$. For $t > 0$, the potential $V(z)$ is turned off, causing the system's Hamiltonian to return to H_1, and the wave function evolves as

$$|\Psi(t)\rangle = \exp(-iH_1 t/\hbar)|\Psi(0)\rangle. \tag{6}$$

In the subsequent analysis, we thoroughly investigate the properties of $|\Psi(t)\rangle$.

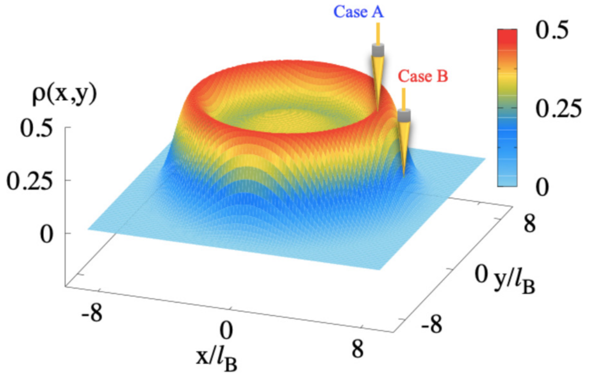

FIG. 2. The electron density profile of the Laughlin state for nine electrons. In two distinct cases, pulse excitations are applied with parameters set to $w = 5.4l_B$(case A) and $w = 7.0l_B$(case B). one corresponds to the spatial location where the edge electron density of the system attains its extremum, while the other is situated in the vicinity of the system boundary.

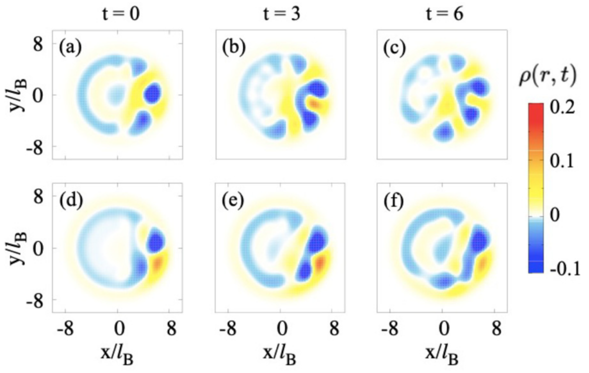

FIG. 3. Evolution of the residual density under quenched dynamics in a system comprising 9 electrons in 27 orbitals, with $\tau = 3$ and $U_\delta = 1$. (a)–(c) depict the dynamic process of edge density diffusing into the bulk over time when the tip potential is at $w = 5.4l_B$; (d)–(f) correspond to $w = 7.0l_B$, where the penetration depth of edge density into the bulk is significantly less than that at $w = 5.4l_B$ on the same time scale, demonstrating that the pulse position modulates the diffusion intensity.

III. QUENCH DYNAMICS AT THE FQH EDGE

The presence of boundaries in the system results in a nonuniform edge electron density distribution of the FQH liquid. This nonuniformity originates from the electron-electron correlation and results in an edge dipole momentum, which is related to the Hall viscosity and topological properties of the FQH liquids [53,54]. Moreover, the edge excitation velocity is defined by the slope of the EMP dispersion in the long-wavelength limit $k \to 0$ [37]. For model Hamiltonian with V_1 interaction, the edge states are also zero-energy eigenstates, and thus the edge velocity is zero. In this scenario, the impact of the tip potential does not propagate along the boundary, meaning that the system does not experience rotation except diffusion over time. To effectively capture the small changes in density evolution, we investigate the time evolution of the electron density diffusion induced by the pulse tip potential with a residual density distribution defined as

$$\rho(r,t) = \langle\Psi(t)|\Psi(t)\rangle - \rho_1, \tag{7}$$

where $\rho_1(r,t) = |\Psi_1|^2$ represents the nonperturbed electron density of the Laughlin state prior to the introduction of the pulse tip potential. Due to the tip potential breaks the rotational symmetry, numerical diagonalization can only be applied to relatively small system sizes. For the Laughlin state at $\nu = 1/3$, we consider a system with $N_e = 9$ electrons in $N_{\text{orb}} = 27$ orbitals. Then the disk has a radius around $R \sim \sqrt{2N_{\text{orb}}} = 7.3l_B$. As depicted in Fig. 2, the electron density maintains a constant value at the disk's center but becomes inhomogeneous toward the edge, reaching a peak around $r \sim 5.4l_B$.

The pulse tip potential is established with a fixed strength of $U_\delta = 1$ and a duration $\tau = 3$. Two values are assigned to position w, namely $w = 5.4l_B$ (case A) and $w = 7.0l_B$ (case B). One corresponds to the density maximum, while the other is situated near the boundary. As shown in Fig. 3, we examine $\rho(t)$ for both cases at several time points. In case A, illustrated in Figs. 3(a)–3(c), when the tip is positioned at the density peak, the residual electron density clearly shows diffusion traits into the bulk. In contrast, as the tip nears the edge, as in case B shown in Figs. 3(d)–3(f), $\rho(t)$ appears to be more concentrated along the edge. This aligns with the experimental findings described in Ref. [44], indicating that the pulse near the edge has the capability to excite both edge waves and bulk modes. However, our simulation reveals that the influence of these two excitations highly depends on the tip position w, as analyzed below. Moreover, when the tip is positioned close to the edge, the excitation should be dominated by edge states, and its dynamics should reveal the corresponding edge velocities. In Appendix C, we compare the dynamics of a well-defined quasihole excitation at the edge and an approximate tip excitation at the edge within a truncated Hilbert space. The resulting edge velocities are in good agreement with those extracted from full Hilbert space time evolution.

Next, we conduct a further investigation of this dynamical process from the perspective of wave functions. Within the framework of this study, the initial state for system evolution is the Laughlin state Ψ_1. Taking a system with the electron number $N_e = 9$ as an example, Ψ_1 corresponds to a zero-energy eigenstate with angular momentum $M_0 = 3N_e(N_e - 1)/2 = 108$. The pulse process, accompanied by energy injection into the system, may induce transitions to high-energy excited states. To quantitatively characterize the quantum transition process from ground state to excited states after pulse application, Fig. 4 presents the energy spectrum of the V_1 Hamiltonian for a system with $N_{\text{orb}} = 27$ orbitals. A color bar illustrates the squared overlap distributions between the post-pulse state $\Psi(0)$ for case A [Fig. 4(a)] or B [Fig. 4(b)] and every state in the energy spectrum. It is shown that the nonzero overlap states are distributed on both sides of the ground state.

The top five largest square overlaps are denoted by the symbol $E_{\alpha i}$. Here, $\alpha \in \{A, B\}$ distinguishes case A from case B, while $i \in \mathbb{N}$ with $1 \leqslant i \leqslant 5$ is an integer index indexing the ranking of overlap strengths. The labeling follows the descending order $E_{\alpha i} > E_{\alpha(i+1)}$. (In Case A, we label both the ground state and the excited states with energy $E > 0$.)

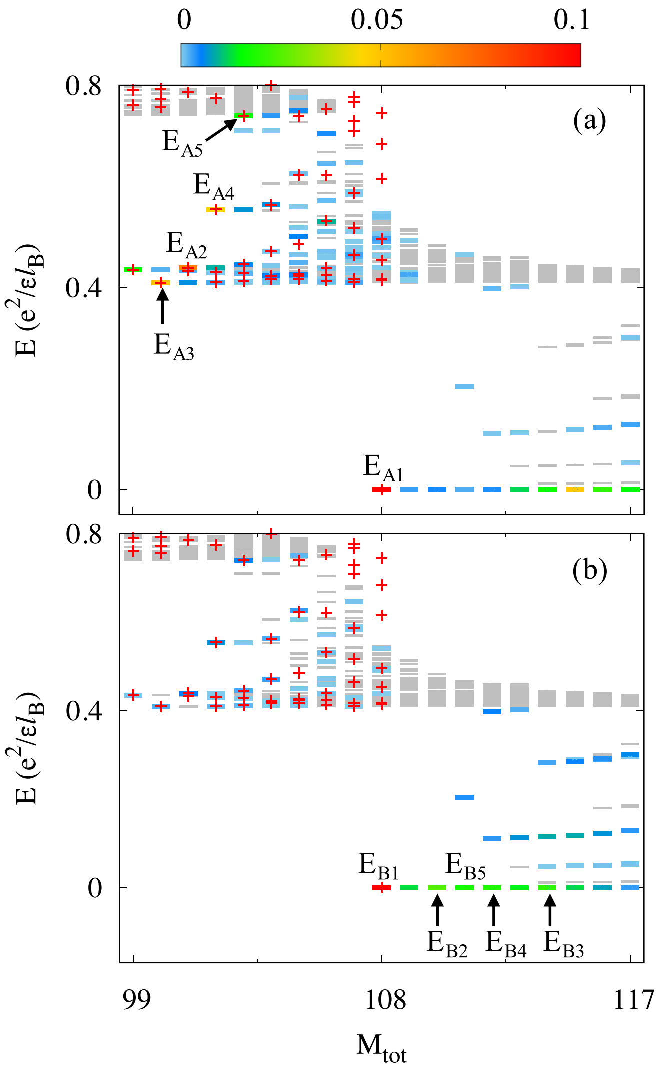

FIG. 4. Energy spectrum for nine electrons and 27 orbitals. A color bar illustrates the squared overlap distributions between the post-pulse state $\Psi(0)$. The states indicated by the red cross points are the eigenstates in the subspace of zero center of mass (COM) angular momentum. The top five maximum square overlaps are labeled as $E_{\alpha i}$, $\alpha \in \{A, B\}$ distinguishes case A/B, and $i \in \{1, 2, 3, 4, 5\}$ denotes the overlap intensity ranking, satisfying the decreasing order $E_{\alpha i} \geqslant E_{\alpha(i+1)}$. (In case A, we label both the ground state and the excited states with energy $E > 0$.) (a) Case A, with the states having higher weights predominantly distributed in the bulk states. (b) Case B, with the states having higher weights predominantly distributed in the edge states.

The states indicated by the red cross points are the eigenstates in the subspace of zero center of mass (COM) angular momentum. The COM operator is characterized as $\hat{M} = \hat{B}^\dagger \hat{B}$, where the ladder operator is given by $\hat{B} = \sum_i \hat{b}_i / N_e$, with $\hat{b}_i$ representing the ladder operator for each guiding center orbital. Our earlier research [55] demonstrates that the neutral magnetoroton excitation mode lives in this subspace, particularly focusing on low-energy states with angular momentum M_{tot} in the range $[M_0 - N_e, M_0]$. In case A, as illustrated in Fig. 4(a), all states with the highest overlap, except the ground state, are located in the left segment of the spectrum among the bulk excited states. In particular, these states with maximal overlap are located within the $M = 0$ subspace and are marked with red cross symbols. They predominantly occupy the low-energy part of the spectrum on this side, implying a significant contribution from the magnetoroton excitation mode. In addition, certain states demonstrating the highest overlap are located in the upper segment of the energy spectrum, such as the E_{A4} state. This excitation could be explained by magnetoroton excitation, where a particle transitions to a higher Λ level within the framework of composite fermion theory [56]. In case B, when the tip is located near the boundary, as shown in Fig. 4(b), the states exhibiting the highest overlap are found among the zero-energy states in the right part of the spectrum, particularly associated with the edge excitation mode of the FQH liquid [9]. The variation observed in the weight distribution illustrates that the excitation of the pulse is significantly influenced by the tip's position.

Now we calculate the post-quench fidelity $f(t) = |\langle\Psi(0)|\Psi(t)\rangle|^2$ to monitor the dynamical evolution. The oscillation period of $f(t)$ is determined by the energy difference between the eigenstates in the energy spectrum. The oscillation amplitude is influenced by the overlap between the initial state $\Psi(0)$ and the eigenstates of the Hamiltonian H_1. Analytically, the fidelity $f(t)$ can be expanded in terms of energy eigenstates as

$$|\langle\Psi(0)|\Psi(t)\rangle|^2 = \left|\sum_i |c_i|^2 e^{-iE_i t/\hbar}\right|^2 = \sum_i |c_i|^4 + \sum_{i<j} 2|c_i|^2|c_j|^2 \cos\left(\frac{(E_i - E_j)t}{\hbar}\right). \tag{8}$$

As shown in Fig. 5(a), $f(t)$ exhibits distinct multiperiod oscillation characteristics. During the initial stage, the fidelity decreases monotonically as the electron density perturbation diffuses into the bulk or along the edge from the tip. After a certain time, the fidelity begins to oscillate, indicating that the electron density wavepacket has re-emerged at the edge. This oscillation behavior is consistent with the periodic diffusion of the electron density wavepacket observed in Fig. 3. The oscillation period is determined by the energy differences between the eigenstates involved in the dynamics. In case A, where the tip is positioned at $w = 5.4 l_B$, the oscillation period is approximately $T \approx 14.3$ (in units of $\hbar \varepsilon l_B / e^2$) corresponding to a frequency of $\Omega \approx 0.44$ which is very close to the energy of the magnetoroton mode in large k limit. The amplitude of these oscillations is relatively large, and the oscillation frequency is relatively high, indicating that the excitation energy is high and that the system diffuses during this process. In contrast, for case B, the fidelity exhibits larger values and slower oscillations, suggesting a greater retention of ground state characteristics, consistent with the tip's proximity to the edge. Furthermore, the observation of long-period oscillations in $f(t)$ indicates lower energy excitations at the FQH edge.

To extract the characteristic oscillation frequencies, we performed a discrete Fourier transform of the fidelity $f(t)$ from Fig. 5(a), with the resulting frequency spectrum $F(\Omega)$ shown in Fig. 5(b). The dominant frequency peaks of case A are concentrated in the high-frequency region with $\Omega \geqslant 0.41$,

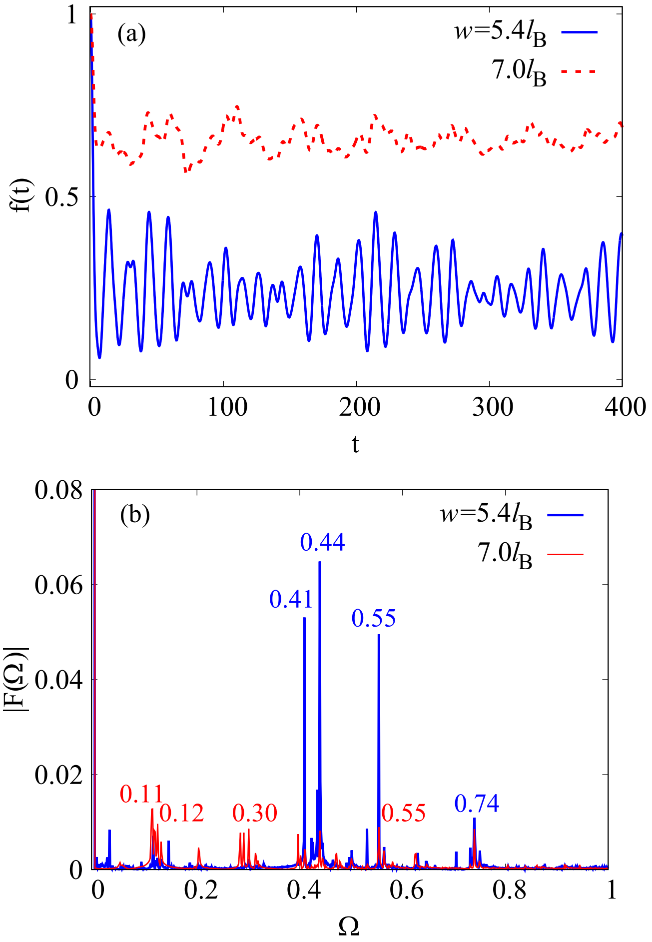

FIG. 5. (a) The evolution of fidelity $f(t)$. In case A at tip position $w = 5.4l_B$, the fidelity oscillations exhibit relatively large amplitudes, and the oscillation frequency is relatively high, indicating high excitation energy. In case B at tip position $w = 7.0l_B$, the fidelity shows larger magnitudes and slower oscillations, suggesting higher retention of ground-state characteristics. This result aligns with the density evolution observations in Fig. 3. (b) The discrete Fourier transform of the fidelity $f(t)$ in Fig. 5(a). The first four largest frequency peaks are marked for each case. The largest frequency peaks of case A are mainly distributed in the region of $\Omega \geqslant 0.41$, while the peaks of case B are concentrated in the range of $\Omega < 0.41$. Notably, the high-frequency interval of $\Omega > 0.41$, the peaks of the two cases overlap.

while the peaks of case B mainly appear in the low-frequency range with $\Omega < 0.41$. Notably, in the interval with $\Omega > 0.41$, the spectral peaks of the two cases show significant overlap. Moreover, the spectral peaks of case A are significantly higher than those of case B, indicating more prominent signal characteristics. Thus our analysis focuses on case A. The spectral peaks of case A correspond to the energy differences in Fig. 4(a), as detailed in Table I. For example, the peak of the fundamental frequency at $\hbar\Omega_{12} = |E_{A1} - E_{A2}| = 0.44$ corresponds to a period $T_{12} = 2\pi/\Omega_{12} \approx 14.3$, and the secondary peak at $\hbar\Omega_{13} = |E_{A1} - E_{A3}| = 0.41$ yields $T_{13} = 2\pi/\Omega_{13} \approx 15.3$. These periodicities quantitatively explain the dominant oscillations observed in Fig. 5(a). Moreover, all identified dominant energy levels coincide with the magnetoroton spectrum in case A, confirming that the oscillation periods of $f(t)$ are governed by these transitions. This indicates that after the edge pulse excitation in the Hall fluid, the electron diffusion into the bulk is directly modulated by the collective modes of the magnetoroton excitations.

TABLE I. The table of absolute value of the energy difference $|E_{Ai} - E_{Aj}|$ marked in Fig. 4(a), where the underlined energy differences correspond to the peak frequencies in the Fourier spectrum of Fig. 5(b).

	E_{A1}	E_{A2}	E_{A3}	E_{A4}	E_{A5}
E_{A1}	0				
E_{A2}	$\underline{0.44}$	0			
E_{A3}	$\underline{0.41}$	0.03	0		
E_{A4}	$\underline{0.55}$	0.11	0.14	0	
E_{A5}	$\underline{0.74}$	0.30	0.33	0.19	0

IV. ANALYZE OF THE DETAILS OF THE TIP

Previously, we discussed the quench dynamics of the edge state induced by a specific pulse potential at the edge of a FQH liquid. The results indicate that the pulse can excite both edge and bulk states, and the excitation characteristics are significantly influenced by the position of the pulse. In this section, we will further analyze the effects of pulse position w, duration τ, and intensity U_δ on excitation characteristics. As shown above, the pulse position is particularly crucial as it determines the initial electron density distribution, which in turn affects the excitation process. The duration and intensity of the pulse also play an important role in determining the amplitude and energy of the excitation. By systematically varying these parameters, we can gain a deeper understanding of how they influence the quench dynamics and the resulting excitation characteristics.

Pulse positon. As described in Sec. III, the pulse position significantly affects the proportion of the post-pulse state $\psi(0)$ excited to bulk states and edge states. To quantitatively analyze the contribution rates of these two types of states to the time evolution, we fix the tip potential parameters of the pulse as strength $U_\delta = 1$ and duration $\tau = 3$, and introduce the bulk contribution S_{bulk} as follows:

$$S_{\text{bulk}} = \sum_{m=M_0-N_e}^{M_0-1} \sum_{i=0}^{39} |\langle\Psi(0)|\phi_{m,i}\rangle|^2, \tag{9}$$

where $\phi_{m,i}$ represents the ith excited state at angular momentum m, with double summation traversing the lowest 40 excited states in each angular momentum sector within the $[M_0 - N_e, M_0 - 1]$ angular momentum window where the magnetoroton excitation lives. The larger the value of S_{bulk}, the more readily the initial state $\Psi(0)$ can be excited into the bulk states within this angular momentum interval, indicating that the system evolution will be significantly governed by the collective modes of magnetoroton. Based on the aforementioned analysis, the pulse position may exert a significant regulatory effect on the diffusion dynamics. To investigate this, we systematically varied the spatial position of the excitation pulse, calculated the dependence of S_{bulk} on the pulse

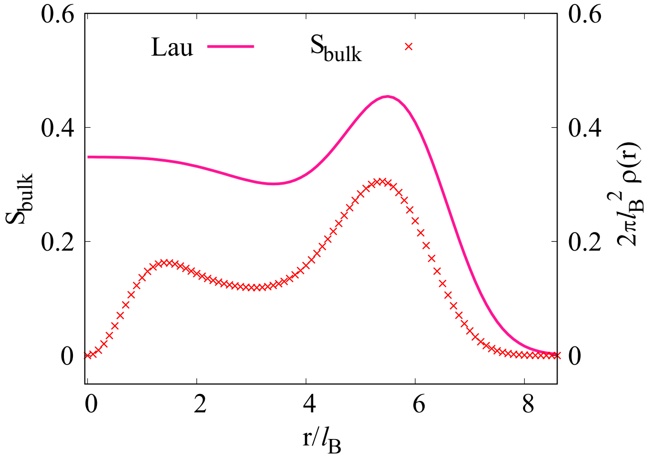

FIG. 6. The dependence of S_{bulk} on the pulse position. The peak location of electron density nearly coincides with the maximal value of S_{bulk}. This correspondence indicates that positioning the excitation pulse near the electron density peak effectively enhances the hybridization effect in the bulk state.

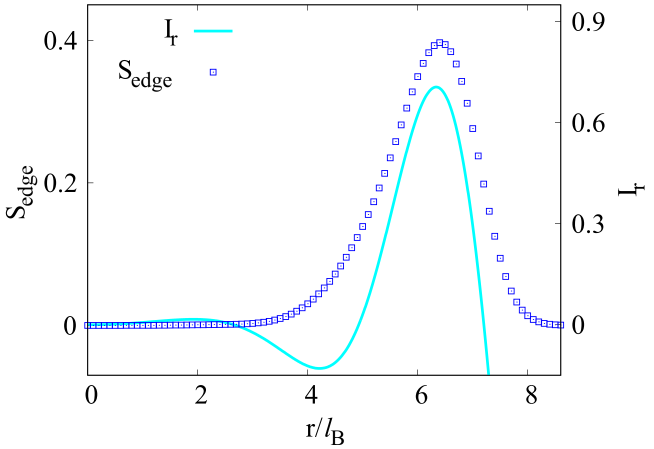

FIG. 7. The pulse position dependence of S_{edge}. S_{edge} exhibits an asymmetric unimodal distribution between $3.2l_B$ and $8.2l_B$, peaking at $r = 6.4l_B$. The solid line represents the dipole moment I_r, also maximized at the same location.

position, and plotted the results in Fig. 6. As shown in the Fig. 6, a prominent maximum of S_{bulk} appears at $r = 5.4l_B$, indicating a significant enhancement effect of the pulse on the diffusion process at this location. Furthermore, the distribution of electron density before the pulse, depicted by the solid line in Fig. 6, reveals that the peak region of the electron density near the edge coincides with the maximum of S_{bulk}. When the pulse position moves toward the edge of the system to $r = 8.0l_B$, the intensity of S_{bulk} gradually decreases to zero, which is consistent with the electron density reaching the physical boundary of the system at this position. In particular, the spatial span from the maximum point to the zero point corresponds exactly to the radius of a quasi-hole, that is, $r \simeq 2.5l_B$ [57–60]. Meanwhile, we can also introduce the edge contribution S_{edge} to quantify the contribution of the edge state to the quench dynamics. Edge states are defined as zero-energy eigenstates in the right part of the energy spectrum, which are typically located in the angular momentum range $[M_0 + 1, M_0 + N_e]$. The edge contribution is defined as

$$S_{\mathrm{edge}} = \sum_{m=M_0+1}^{M_0+N_e} \sum_{i=0}^{n} |\langle\Psi(0)|\phi_{m,i}\rangle|^2. \tag{10}$$

The truncation parameter n is determined by the energy gap between the ground state and the bulk states. For the $V_1 = 1$ model Hamiltonian, the energy gap $\Delta E \approx 0.41$, and n is taken as the number of edge states with energies below ΔE. The parameter S_{edge} quantifies the percentage proportion of edge states involved in the quench dynamics after the termination of the pulse. The ratio between S_{bulk} and S_{edge} directly reflects the competitive relationship between the bulk and edge states during the evolution process. Similarly, we calculated the dependence of S_{edge} on the pulse position, as shown in Fig. 7. Unlike S_{bulk}, S_{edge} exhibits accumulation only within a specific edge-confined region. Specifically, as the probe moves from $r = 3.2l_B$ toward the edge, S_{edge} increases monotonically, reaches a maximum at $r = 6.4l_B$, then rapidly decays to zero at $r = 8.2l_B$. This indicates that the pulse position significantly influences the excitation of edge states, with the maximum excitation occurring at $r = 6.4l_B$. In order to further understand the position of the maxima excitation, we analyze the dipole moment of the edge state. The dipole moment is a measure of the asymmetry of the electron density distribution at the edge, which is closely related to the quasiparticle excitation. It is defined as $I_r = \int_0^r r(\rho(r) - \nu)dr$. As shown in Fig. 7, it is interesting that the dipole moment I_r also exhibits a maximum at $r = 6.4l_B$, which coincides with the position of the maximum contribution of the edge excitations. This indicates that the pulse position at $r = 6.4l_B$ corresponds to the point where the electron density distribution is most asymmetric, leading to particle-hole pairing excitation near the edge. Additionally, the S_{edge} extends roughly $5l_B$, matching the quasihole diameter or the particle-hole pair's central distance [57–60].

In conclusion, the pulse position dependence of S_{edge} indicates that the excitation of edge states is highly sensitive to the position of the pulse. When the pulse is applied at the edge, the edge states are excited, which is closely related to the quasiparticle excitation, leading to a significant increase in S_{edge}. In contrast, when the pulse is applied to the center of the disk, the edge states are not excited and S_{edge} is zero.

Pulse duration and strength. In the experiment, pulse duration τ and strength U_δ are adjustable parameters. We analyzed the effect of pulse duration on excitation by calculating $|\langle\Psi(0)|\Psi_1\rangle|^2$ versus U_δ for various τ. Figure 8 shows that $|\langle\Psi(0)|\Psi_1\rangle|^2$ varies periodically with U_δ with a slowly decaying amplitude, particularly for small τ. Moreover, τ and the oscillation period ΔU_δ show an inverse relationship: $\Delta U_\delta \cdot \tau = 2\pi$. This means that varying ΔU_δ or varying τ yields similar effects. Treating all excited states, excluding only the ground state $|\Psi_1\rangle$ before applying the pulse, as a single system excitation, this oscillation is very likely the Rabi oscillation in a two-level system with a gap U_δ. The transition probability is proportional to $|\sin(U_\delta\tau/2)|^2$ and thus U_δ is periodic with $2\pi\hbar/\tau$ for a fixed τ. Thus the ground state

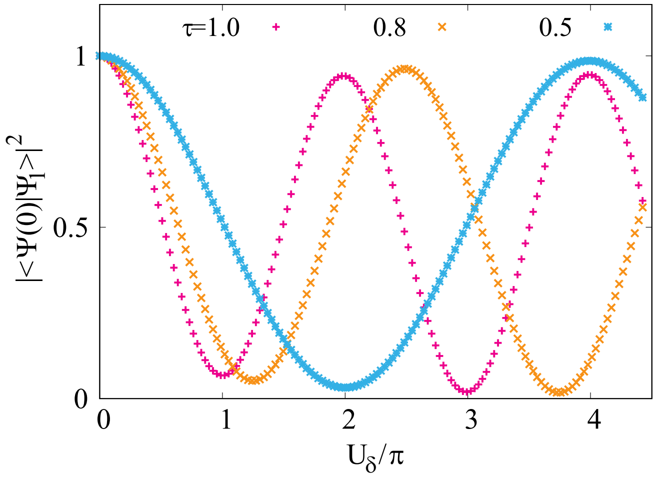

FIG. 8. Variations of the wavefunction overlap $|\langle\Psi(0)|\Psi_1\rangle|^2$ as a function of the pulse strength U_δ for various τ in the nine-electron, 27-orbital system with $w = 5.4l_B$.

excitation can be adjusted by the pulse duration τ and the strength U_δ.

V. DISCUSSIONS AND CONCLUSIONS

In this work, we have investigated the quench dynamics of edge excitations in FQH liquid at the filling factor $\nu = 1/3$ motivated by recent pump probe reflectance measurements in time-resolved photoluminescence spectroscopy. By applying a tip potential to the edge of the Hall liquid, we simulate an electrical pulse that excites the Laughlin state into the energy spectrum branch of the edge mode and magnetoroton. The electron density evolution reveals that due to chiral edge modes, electrons move along the edge while also diffusing into the bulk. We calculated the fidelity after quenching and performed spectral analysis on the time-dependent fidelity. The results show that the evolution frequency aligns with the energy gap of the magnetoroton, and electron diffusion into the bulk is attributed to the winding of the magnetoroton. In addition, we discussed how the location, intensity, and duration of the pulse affect the quench dynamics. The results indicate that the position of the pulse significantly influences the excitation characteristics, with the maximum excitation occurring when the pulse is applied at the peak of the electron density. The duration and intensity of the pulse also play crucial roles in determining the amplitude and energy of the excitation. The periodic nature of the excitation suggests that the system can be tuned to achieve optimal excitation conditions by adjusting these parameters. In conclusion, our study offers insights into multiple aspects of the quench dynamics of edge excitations in FQH liquids. The results highlight the importance of the pulse position, duration, and intensity in controlling the excitation characteristics. This work initiates further investigations into the dynamics of edge excitations in more exotic FQH systems and their potential applications in quantum information processing and quantum simulation.

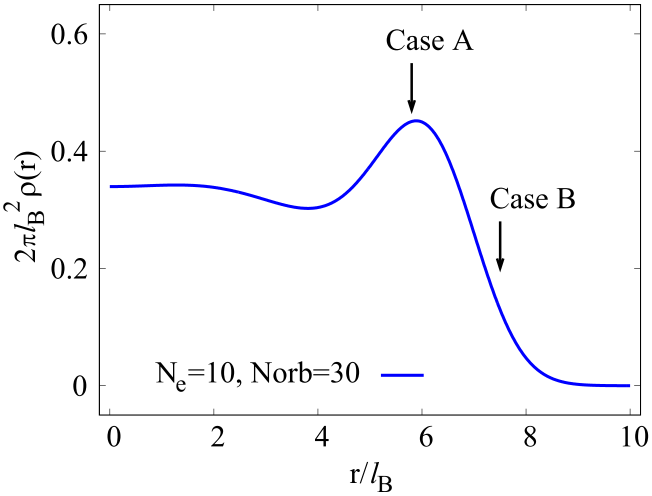

FIG. 9. Radial density distributions for a system of 10 electrons occupying 30 orbitals. The tip potential positions are set at $w = 5.8l_B$ for Case A and $w = 7.5l_B$ for case B, respectively.

ACKNOWLEDGMENTS

We thank H.-T. Lu for the help of the time-dependent Lanczos algorithm. This work was supported by the National Natural Science Foundation of China Grants No. 12474140 and No. 12547101.

DATA AVAILABILITY

The data that support the findings of this article are openly available [61].

In the Appendix, we present data for 10 electrons, the effect of realistic Coulomb interactions, and the dynamics in a truncated space compared to the case where the tip is located at the edge.

APPENDIX A: THE DYNAMICS OF SHORT-RANGE INTERACTIONS IN A 10-ELECTRON SYSTEM

Consistent with the analysis logic of the nine-electron system in the main text, two different cases are selected to observe the evolution of residual density. For the $N_e = 10$, $N_{\mathrm{orb}} = 30$ system in this Appendix, the radius $R \sim \sqrt{2N_{\mathrm{orb}}} \approx 7.75\ l_B$. To assess how the tip potential position influences residual density evolution, two cases are established. Case A places the tip at $w = 5.8l_B$, the electron density peak near the edge; case B positions it at $w = 7.5l_B$, close to the physical boundary, as shown in Fig. 9. Both cases use fixed pulse parameters: $\tau = 3$ and $U_\delta = 1$.

For short-range interaction, the residual electron density is measured at three points: $t = 0$, 3, and 6 [see Fig. 10]. Case A [Figs. 10(a)–10(c)]: As time progresses, residual density diffuses significantly into the bulk, matching the 9-electron system trend at $w = 5.4l_B$ in the main text. Case B [Figs. 10(d)–10(f)]: At the same time scale, the residual density's penetration into the bulk is much less than in case A, confirming the tip position's impact on diffusion intensity.

We also examine the energy spectrum of a ten-electron system under short-range interactions by calculating the squared

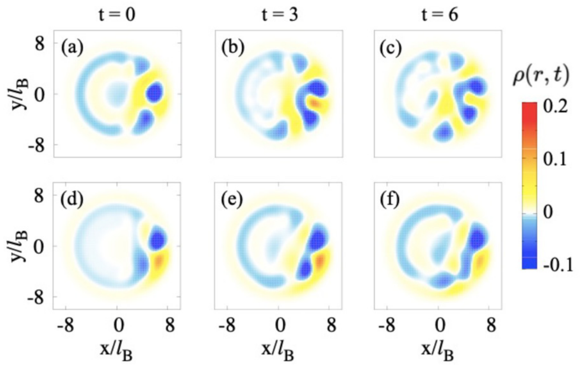

FIG. 10. Evolution of the residual density under quenched dynamics in a system comprising 10 electrons in 30 orbitals, with $\tau = 3$ and $U_\delta = 1$. (a)–(c) Case A depicts the dynamic process of edge density diffusing into the bulk over time when the tip potential is at $w = 5.8 l_B$; (d)–(f) Case B corresponds to $w = 7.5 l_B$, where the penetration depth of edge density into the bulk is significantly less than that at $w = 5.8 l_B$ on the same time scale, demonstrating that the pulse position modulates the diffusion intensity.

overlap between the post-pulse state $\Psi(0)$ and each eigenstate, shown in Fig. 11. In case A, high overlap states appear in both bulk and edge states, while in case B, they concentrate mainly in edge states. This mirrors the nine-electron system results (Fig. 4), showing that the principle of tip potential affecting excitation ratios remains consistent when scaling from nine to ten electrons.

To test the pulse response universality across system sizes, we compared the squared overlap between the initial and ground states in nine and ten electron systems by varying pulse intensity and duration. Figure 12 displays the results: solid symbols for nine electrons and hollow for ten. Both systems show notable periodic oscillations with high overlap, indicating minimal influence of system size on the squared overlap pattern.

APPENDIX B: THE EFFECT OF COULOMB INTERACTIONS

In the above analysis, we have considered the short-range interaction V_1 in the Hamiltonian, which is a good approximation for the Laughlin state. However, in reality, the Coulomb interaction leads to a more complex energy spectrum and can modify the excitation energies of the system. Therefore, we consider the following hybrid Hamiltonian:

$$H_1 = (1 - \lambda V_{C1}) V_1 + \lambda H_C, \tag{B1}$$

where V_1 is the model Hamiltonian, V_{C1} denotes the first pseudopotential coefficient of the Coulomb interaction, and H_C represents the Coulomb interaction Hamiltonian. It ensures $V_1 = 1$ which makes the results comparable to the pure V_1 case. The Coulomb Hamiltonian is

$$H_C = \sum_{m_1 m_2 m_3 m_4} V_{1234} C^\dagger_{m_1} C^\dagger_{m_2} C_{m_3} C_{m_4} + \sum_m U_m C^\dagger_m C_m. \tag{B2}$$

The first term includes the electron-electron Coulomb interaction, and the second one represents the background

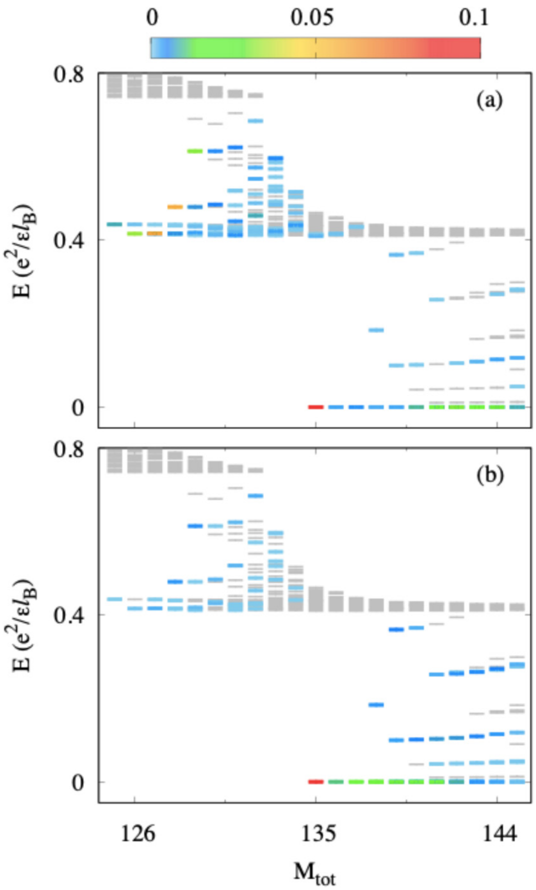

FIG. 11. Energy spectrum of a ten-electron system with V_1 interactions. The color bar represents the intensity of the squared overlap between the post-pulse state $\Psi(0)$ and each eigenstate. (a) Case A: high-weight states are mainly distributed in both the bulk state region and the edge state region. (b) Case B: high-weight states are concentrated in the edge state region.

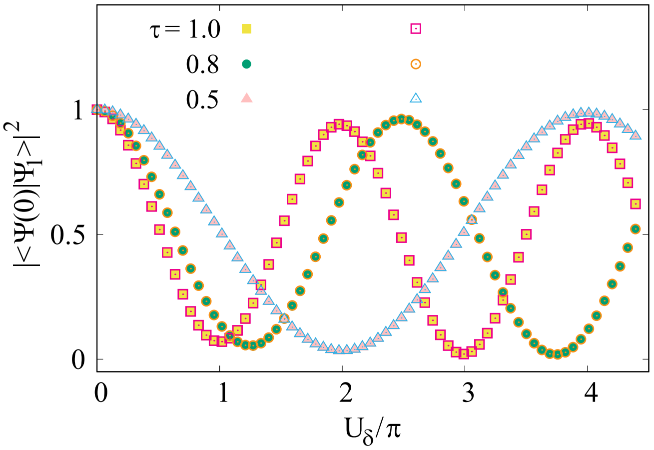

FIG. 12. The impact of $|\langle\Psi(0)|\Psi_1\rangle|^2$ on pulse intensity U_δ is shown with a fixed pulse duration of $\tau = 3$. Tip potential is set to $w = 5.4\ l_B$ for the nine-electron system (solid symbols) and $w = 5.8\ l_B$ for the ten-electron system (hollow symbols).

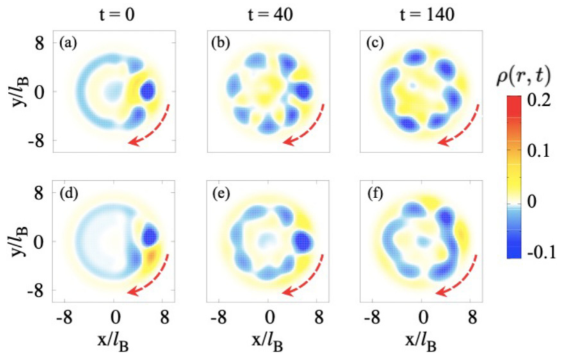

FIG. 13. Evolution of residual density in a nine electron, 27 orbital system under mixed Coulomb interactions with $\tau = 3$ and $U_\delta = 1$: The edge density diffuses inward into the bulk and propagates clockwise along the boundary. The red arrow indicates edge movement direction. [(a)–(c)] Case A shows inward diffusion and edge propagation over time with tip potential at $w = 5.4l_B$. [(d)–(f)] Case B shows clockwise edge propagation with less bulk penetration compared to $w = 5.4l_B$ at the same time scale.

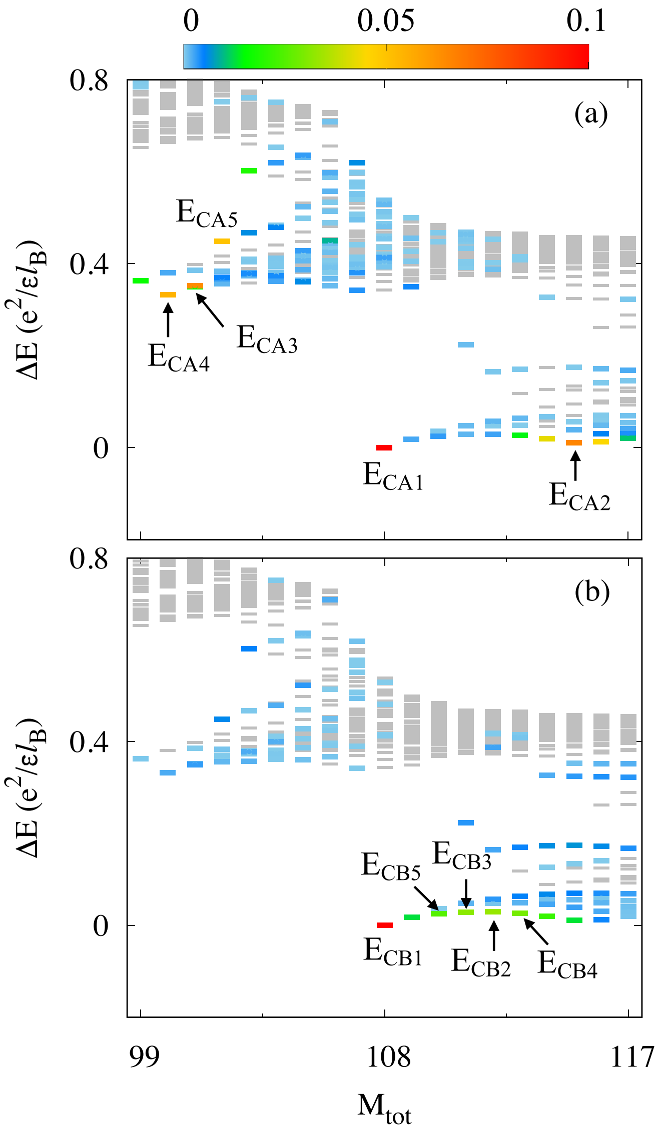

FIG. 14. Energy spectrum of mixed Coulomb interactions with $\lambda = 0.6$. Edge states have a structured energy level instead of zero energy. The color bar shows the overlap integral between the post-pulse state and spectral states. The top five states by squared overlap are labeled $E_{C\alpha i}$, distinguished by $\alpha \in \{A, B\}$ for cases A/B, with $i \in \{1, 2, 3, 4, 5\}$ for ranking (in decreasing order $E_{C\alpha i} \geqslant E_{C\alpha(i+1)}$). (a) In case A, apart from the ground state at angular momentum 108, the high-weight states are mainly in the angular momentum spaces 115, 100, 101, and 102. (b) In the case B, they are mainly near the edge states next to the angular momentum space 108.

confinement [22]. Parameter λ denotes the weights of long-range interactions.

As an example, we set $\lambda = 0.6$ to incorporate the influence of the Coulomb effect. In this context, $V(z)$ in Eq. (4) is still applicable, but the Hamiltonian H_1 changes to Eq. (B1). We calculated the quench dynamics for nine electrons in 27 orbitals with $\tau = 3$ and $U_\delta = 1$. In this case, we have position $w = 5.4l_B$(case A) and $w = 7.0l_B$(case B). We monitored the residual electron density at time points $t = 0,\ 40,$ and 140. As shown in Fig. 13, the evolution of the residual density shows that the edge density simultaneously penetrates into the bulk region and propagates clockwise along the boundary. Figures 13(a)–13(c) display the dynamic process of the residual density over time for case A. Figures 13(d)–13(f) correspond to the case B. In this case, the residual density propagates clockwise along the boundary, but its penetration depth into the bulk is less than that of case A on the same time scale. Similar to the short-range interaction, the pulse acting on the edge causes the remaining density to diffuse into the bulk, and the diffusion depth is regulated by the pulse position. This indicates that the dynamic behavior under more realistic Coulomb interactions exhibits similar qualitative characteristics to the short-range interaction system.

Next, we analyze the influence of the Coulomb interaction on the quench dynamics from the perspective of the energy spectrum. First, we calculate the overlap distribution between the post-pulse state $\Psi(0)$ and the eigenstates of the Hamiltonian (B1). Figure 14 shows the energy spectrum of the Hamiltonian with mixed Coulomb interaction in a nine-electron system. The color bar represents the squared overlap distribution between the post pulse state $\Psi(0)$ and each state in the energy spectrum. As shown in Fig. 14, the color bar indicates that states with relatively large overlap integrals are mainly distributed in the bulk states and edge states, and this distribution characteristic is consistent with short-range interactions. In addition, the energy gap between the edge states and the ground state is significantly smaller than the energy gap between the ground state and the bulk states, which will lead to the evolution period dominated by edge states being longer than that dominated by bulk states. Due to the introduction of long-range Coulomb interactions, the edge states are no longer zero-energy states but dispersive. The nonzero dispersion of the edge states results in nonzero edge velocity [37], which also explains the phenomenon of residual density propagating along the boundary observed in Fig. 13. We label the top five states with the largest squared overlap values as $E_{C\alpha i}$, where $\alpha \in \{A, B\}$ distinguishes the cases A/B, and $i \in \{1, 2, 3, 4, 5\}$ indicates the order of overlap strength (satisfying the descending order $E_{C\alpha i} \geqslant E_{C\alpha(i+1)}$).

In case A ($w = 5.4l_B$), besides the ground state at angular momentum 108, the high-weight states of edge states are mainly concentrated in the region near angular momentum 115, while the high-weight states in bulk states are distributed in the range of angular momenta 100, 111, and 112. In case B ($w = 7.0l_B$), the high-weight states are mainly distributed in the angular momentum interval [108,117], and clustered in the edge state region near $M_{tot} = 108$ in angular momentum space. When the tip potential moves from the edge of the disk towards the center, the weight distribution of edge states shows a trend of migrating from near M_0 to $M_0 + N_e$, which is similar to the radial migration process of quasi-holes on the disk [60]. From the distribution pattern of high-weight states in the energy spectrum, it can be seen that for both case A and case B, the distribution patterns of long-range interactions and short-range interactions are similar.

In summary, introducing Coulomb interaction alters edge states from zero energy, resulting in nonzero edge velocity and enabling density modulations to propagate, complicating quench dynamics. It also complicates the bulk energy spectrum, affecting fidelity oscillation. Numerical diagonalization shows the spectrum's complexity increases, but the qualitative behavior aligns with short-range interaction, affirming its suitability for studying edge quench dynamics in FQH liquids. Qualitatively analogous results are observed in larger systems, e.g., the ten-electron system.

For the quantification of edge-mode velocities, we adopt two independent methods: calculations based on the energy spectrum dispersion relation and velocity estimation based on residual density evolution. These two methods realize the characterization of velocity from the aspects of static energy spectrum and dynamic evolution, respectively.

After the tip potential is removed, for the system with nine electrons, 27 orbitals, $\tau = 3$, $U_\delta = 1$, and $w = 7.0l_B$, we tune the edge-state energy gap by introducing a linear potential $V(r) = \beta r^2/2$ in the angular momentum space (with $\beta = 0.02$), and the obtained edge excitation energy spectrum is shown in Fig. 15(a). Referring to the energy spectrum velocity definition method proposed by Ref. [37], we derive the velocity formula using the energy dispersion relation of edge excitations: $v = (R/\hbar) \cdot \frac{\Delta E}{\Delta M}$, where $\Delta M = M_{\text{tot}} - M_0$, $R = \sqrt{2N_{\text{orb}}}$ is the system edge radius, and ΔE is the edge excitation energy difference corresponding to the angular momentum change $\Delta M = 1$. Substituting the data into the formula, we calculate $v = 0.28025\, e^2/(\epsilon\hbar)$. For a GaAs system, the dielectric constant $\epsilon \approx 13$, and the converted velocity is approximately 4.71615×10^6 cm/s.

Under the same parameters, we further quantify the velocity by tracking the time evolution of the characteristic extreme point in the residual density distribution, i.e., the lowest point of the edge density after pulse excitation, and the relevant results are shown in Fig. 15(b). The inset in the figure displays the density distributions at three moments $t = 0$, 8, and 16, with red triangles marking the positions of the lowest density point at each moment; the rotation angle θ of this lowest point is defined as the angle with the x axis, and its time evolution is characterized by solid red dots. By performing a linear fit to $\theta(t)$, the fitting result is obtained as $\theta(t) = -0.024(\pm 0.001)t + 0.123(\pm 0.007)$, from which the angular velocity $\omega = -0.024(\pm 0.001)$ can be extracted. The negative sign indicates that the density propagates clockwise along the edge. Combining the correlation formula between linear velocity and angular velocity $v = \omega \cdot r$, considering that the pulse acts on $w = 7l_{\text{B}}$, the radius of Laughlin quasiholes is approximately $2.5l_{\text{B}}$, and the radius of quasiholes under Coulomb interaction is about $4l_{\text{B}}$ [62], the actual effective radius r in the mixed interaction considered in our work is taken in the range $w \pm 3l_{\text{B}}$. Based on this, the calculated range of the edge propagation linear velocity is 1.5482×10^6 cm/s $\sim$ 4.207×10^6 cm/s, which is of the same order of magnitude as the result obtained by the energy spectrum analysis method, verifying the consistency of the velocity quantification results.

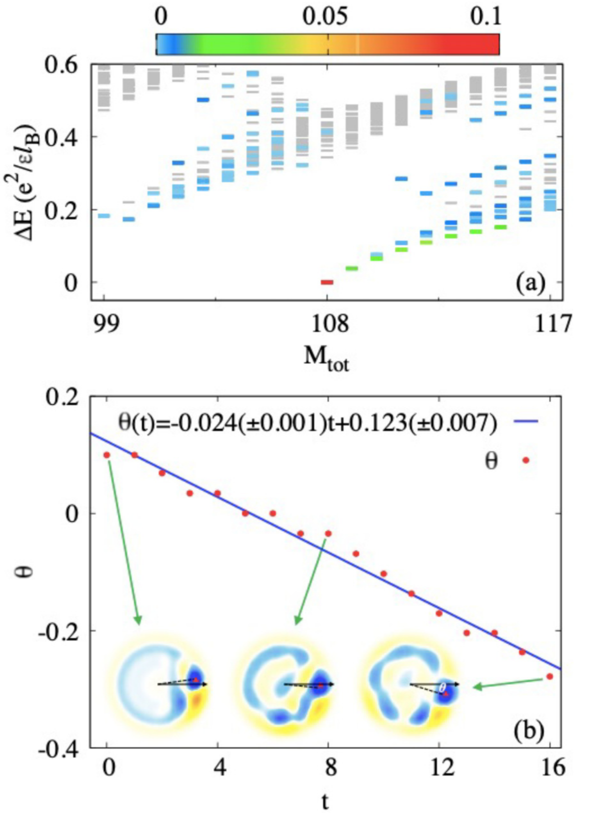

FIG. 15. (a) Energy spectrum under mixed Coulomb interaction with the inclusion of a linear potential, where $\lambda = 0.6$ and $\beta = 0.02$. (b) Time evolution of the rotation angle θ of the lowest point in the residual density. The inset shows the density distributions at three moments $t = 0$, 8, and 16, with red triangles marking the positions of the lowest density point at each moment.

APPENDIX C: EDGE DYNAMICS IN TRUNCATED SPACE

To clarify the validity of the edge-state-dominated evolution and corroborate the effectiveness of the edge-state subspace projection method, we supplement two numerical verification approaches in this Appendix. These approaches explicitly demonstrate the consistency between the evolution results in the projected edge-state subspace and those from the full-space time evolution in the regime of weak bulk-edge hybridization. The details are presented as follows:

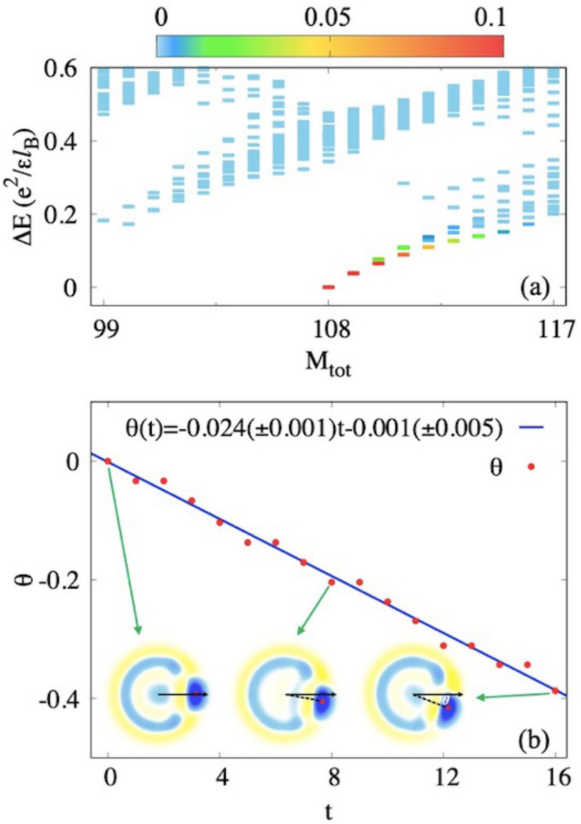

FIG. 16. (a) Projection of the initial quasihole state localized at $w = 7.0l_B$ onto the edge excitation energy spectrum under the Coulomb interaction ($\lambda = 0.6$) and linear potential ($\beta = 0.02$). The quasihole state is entirely distributed in the edge-state subspace. (b) Time evolution of the rotation angle θ of the lowest point in the residual density of the quasihole state. The inset shows the density distributions at $t = 0,\ 8,$ and 16, with red triangles marking the position of the lowest density point at each moment.

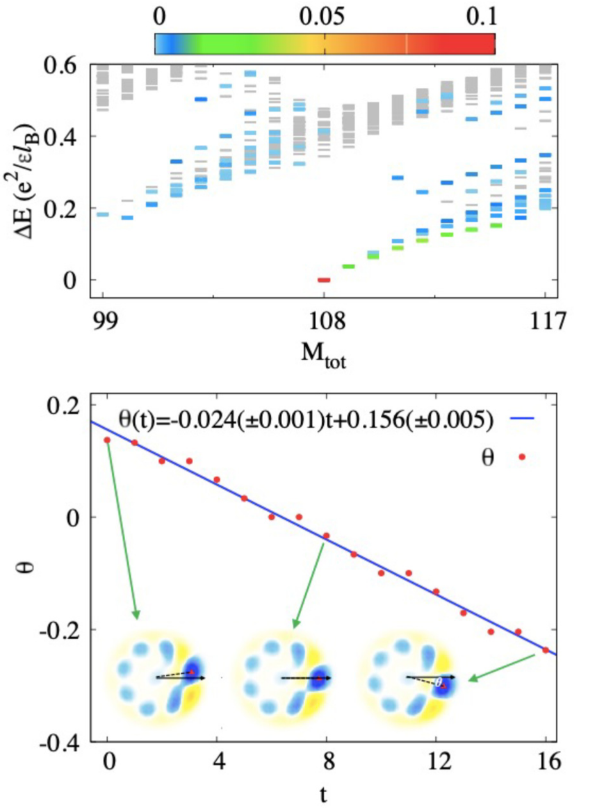

FIG. 17. (a) Edge excitation energy spectrum under the Coulomb interaction ($\lambda = 0.6$) and linear potential ($\beta = 0.02$). All states with a squared overlap weight greater than 0.01 with the post-pulse state are distributed in the edge-state subspace. (b) Time evolution of the rotation angle θ of the lowest point in the residual density under the restricted evolution in the edge-state subspace. The inset shows the density distributions at $t = 0,\ 8,$ and 16, with red triangles marking the position of the lowest density point at each time.

Time evolution of a quasihole state constructed by a linear combination of edge states. Although the pump-probe process cannot generate a well-defined quasihole or quasiparticle excitation, as an approximation, we follow the previous work Ref. [60], in which the quasihole state was strictly projected onto the edge-state subspace. We construct a quasihole state localized at $w = 7.0l_B$ and perform its time evolution under the same Coulomb interaction parameter ($\lambda = 0.6$) and linear potential ($\beta = 0.02$) as those used in Fig. 15.

As shown in Fig. 16(a), the quasihole state is fully projected onto the edge-state subspace. Using the velocity calculation method in Appendix B, we extract the edge excitation velocity from the edge spectrum [Fig. 16(a)], and the obtained velocity is $v = 0.28025e^2/(\epsilon\hbar)$. For a GaAs system with a dielectric constant $\epsilon \approx 13$, this velocity is converted to a linear velocity of approximately 4.71615×10^6 cm/s. As shown in Fig. 16(b), the quasihole state exhibits a clockwise time evolution characteristic, which is consistent with the evolution trend shown in Fig. 15(b). Meanwhile, using the tracking method adopted in this work, we track the rotation angle θ of the lowest point in the residual density of the evolving quasihole state [Fig. 16(b)] and fit its time dependence, yielding an angular velocity of $\omega = -0.024\,(\pm 0.001)$. Considering the size of the quasihole (roughly $4l_B$ in the Coulomb case [62]), the edge velocity extracted from the time evolution of the quasihole state is about 1.5482×10^6 cm/s $\sim 4.207 \times 10^6$ cm/s, which is consistent with that from the full-space time evolution in this work.

Time evolution with truncated basis. If we assume the time-dependent tip excitation is simply a combination of high-energy states rather than a well-defined localized quasihole, as another approximation, we filter the eigenstates that have an overlap greater than 0.01 with the post-pulse state in Fig. 15(a) as the evolution basis set. Notably, in the regime of weak bulk-edge hybridization (with the tip potential at $w = 7.0l_B$), all these high-weight states lie within the edge-state subspace.

We perform the time evolution of the post-pulse state using only the truncated edge-state basis and track the dynamic behavior of the residual density. As shown in the inset of Fig. 17(b), the minimum point of the residual density exhibits distinct clockwise rotational propagation along the edge with time evolution, which is consistent with the full-space evolution characteristic. Fitting the time dependence of the rotation angle θ of the minimum point gives the same angular velocity $\omega = -0.024\,(\pm 0.001)$ as that obtained from the quasihole state evolution and the full-space time evolution.

These results are in good agreement with the velocity extracted from full Hilbert space time evolution in the manuscript. When the tip potential is located near the physical boundary, the density evolution is dominated by edge modes, and their propagation velocity should match the edge velocity, as we demonstrate. In contrast, when the tip potential is positioned at the electron density peak—a regime with strong bulk-edge hybridization—the approximated method is no longer applicable.

[1] D. C. Tsui, H. L. Stormer, and A. C. Gossard, Two-dimensional magnetotransport in the extreme quantum limit, Phys. Rev. Lett. **48**, 1559 (1982).

[2] R. B. Laughlin, Anomalous quantum Hall effect: An incompressible quantum fluid with fractionally charged excitations, Phys. Rev. Lett. **50**, 1395 (1983).

[3] F. Wilczek, Quantum mechanics of fractional-spin particles, Phys. Rev. Lett. **49**, 957 (1982).

[4] B. I. Halperin, Statistics of quasiparticles and the hierarchy of fractional quantized Hall states, Phys. Rev. Lett. **52**, 1583 (1984).

[5] D. Arovas, J. R. Schrieffer, and F. Wilczek, Fractional statistics and the quantum Hall effect, Phys. Rev. Lett. **53**, 722 (1984).

[6] A. Y. Kitaev, Fault-tolerant quantum computation by anyons, Ann. Phys. **303**, 2 (2003).

[7] C. Nayak, S. H. Simon, A. Stern, M. Freedman, and S. Das Sarma, Non-Abelian anyons and topological quantum computation, Rev. Mod. Phys. **80**, 1083 (2008).

[8] X. G. Wen, Theory of the edge states in fractional quantum Hall effects, Int. J. Mod. Phys. B **06**, 1711 (1992).

[9] X. G. Wen, Chiral Luttinger liquid and the edge excitations in the fractional quantum Hall states, Phys. Rev. B **41**, 12838 (1990).

[10] S. M. Girvin, A. H. MacDonald, and P. M. Platzman, Collective-excitation gap in the fractional quantum Hall effect, Phys. Rev. Lett. **54**, 581 (1985).

[11] S. M. Girvin, A. H. MacDonald, and P. M. Platzman, Magneto-roton theory of collective excitations in the fractional quantum Hall effect, Phys. Rev. B **33**, 2481 (1986).

[12] B. Yang, Z.-X. Hu, Z. Papić, and F. D. M. Haldane, Model wave functions for the collective modes and the magnetoroton theory of the fractional quantum Hall effect, Phys. Rev. Lett. **108**, 256807 (2012).

[13] A. Chandran, M. Hermanns, N. Regnault, and B. A. Bernevig, Bulk-edge correspondence in entanglement spectra, Phys. Rev. B **84**, 205136 (2011).

[14] Z.-X. Luo, B. G. Pankovich, Y. Hu, and Y.-S. Wu, Correspondence between bulk entanglement and boundary excitation spectra in two-dimensional gapped topological phases, Phys. Rev. B **99**, 205137 (2019).

[15] H. Sahasrabudhe, B. Novakovic, J. Nakamura, S. Fallahi, M. Povolotskyi, G. Klimeck, R. Rahman, and M. J. Manfra, Optimization of edge state velocity in the integer quantum Hall regime, Phys. Rev. B **97**, 085302 (2018).

[16] Y. Ji, Y. Chung, D. Sprinzak, M. Heiblum, D. Mahalu, and H. Shtrikman, An electronic Mach–Zehnder interferometer, Nature (London) **422**, 415 (2003).

[17] J. Nakamura, S. Fallahi, H. Sahasrabudhe, R. Rahman, S. Liang, G. C. Gardner, and M. J. Manfra, Aharonov–Bohm interference of fractional quantum Hall edge modes, Nat. Phys. **15**, 563 (2019).

[18] J. Nakamura, S. Liang, G. C. Gardner, and M. J. Manfra, Direct observation of anyonic braiding statistics, Nat. Phys. **16**, 931 (2020).

[19] H. Bartolomei, M. Kumar, R. Bisognin, A. Marguerite, J.-M. Berroir, E. Bocquillon, B. Plaçais, A. Cavanna, Q. Dong, U. Gennser, Y. Jin, and G. Fève, Fractional statistics in anyon collisions, Science **368**, 173 (2020).

[20] A. H. MacDonald, Edge states in the fractional-quantum-Hall-effect regime, Phys. Rev. Lett. **64**, 220 (1990).

[21] C. d. C. Chamon and X. G. Wen, Sharp and smooth boundaries of quantum Hall liquids, Phys. Rev. B **49**, 8227 (1994).

[22] X. Wan, E. H. Rezayi, and K. Yang, Edge reconstruction in the fractional quantum Hall regime, Phys. Rev. B **68**, 125307 (2003).

[23] X. Wan, K. Yang, and E. H. Rezayi, Reconstruction of fractional quantum Hall edges, Phys. Rev. Lett. **88**, 056802 (2002).

[24] Z.-X. Hu, R. N. Bhatt, X. Wan, and K. Yang, Realizing universal edge properties in graphene fractional quantum Hall liquids, Phys. Rev. Lett. **107**, 236806 (2011).

[25] R. Sabo, I. Gurman, A. Rosenblatt, F. Lafont, D. Banitt, J. Park, M. Heiblum, Y. Gefen, V. Umansky, and D. Mahalu, Edge reconstruction in fractional quantum Hall states, Nat. Phys. **13**, 491 (2017).

[26] C. L. Kane and M. P. A. Fisher, Transmission through barriers and resonant tunneling in an interacting one-dimensional electron gas, Phys. Rev. B **46**, 15233 (1992).

[27] C. de C. Chamon and X. G. Wen, Resonant tunneling in the fractional quantum Hall regime, Phys. Rev. Lett. **70**, 2605 (1993).

[28] C. L. Kane and M. P. A. Fisher, Nonequilibrium noise and fractional charge in the quantum Hall effect, Phys. Rev. Lett. **72**, 724 (1994).

[29] K. Moon, H. Yi, C. L. Kane, S. M. Girvin, and M. P. A. Fisher, Resonant tunneling between quantum Hall edge states, Phys. Rev. Lett. **71**, 4381 (1993).

[30] X. Lin, C. Dillard, M. A. Kastner, L. N. Pfeiffer, and K. W. West, Measurements of quasiparticle tunneling in the $\upsilon = \frac{5}{2}$ fractional quantum Hall state, Phys. Rev. B **85**, 165321 (2012).

[31] A. Bid, N. Ofek, H. Inoue, M. Heiblum, C. L. Kane, V. Umansky, and D. Mahalu, Observation of neutral modes in the fractional quantum Hall regime, Nature (London) **466**, 585 (2010).

[32] M. Wassermeier, J. Oshinowo, J. P. Kotthaus, A. H. MacDonald, C. T. Foxon, and J. J. Harris, Edge magnetoplasmons in the fractional-quantum-Hall-effect regime, Phys. Rev. B **41**, 10287 (1990).

[33] R. C. Ashoori, H. L. Stormer, L. N. Pfeiffer, K. W. Baldwin, and K. West, Edge magnetoplasmons in the time domain, Phys. Rev. B **45**, 3894 (1992).

[34] N. B. Zhitenev, R. J. Haug, K. v. Klitzing, and K. Eberl, Time-resolved measurements of transport in edge channels, Phys. Rev. Lett. **71**, 2292 (1993).

[35] I. L. Aleiner and L. I. Glazman, Novel edge excitations of two-dimensional electron liquid in a magnetic field, Phys. Rev. Lett. **72**, 2935 (1994).

[36] G. Ernst, N. B. Zhitenev, R. J. Haug, and K. von Klitzing, Dynamic excitations of fractional quantum Hall edge channels, Phys. Rev. Lett. **79**, 3748 (1997).

[37] Z.-X. Hu, E. H. Rezayi, X. Wan, and K. Yang, Edge-mode velocities and thermal coherence of quantum Hall interferometers, Phys. Rev. B **80**, 235330 (2009).

[38] R. Bhattacharyya, M. Banerjee, M. Heiblum, D. Mahalu, and V. Umansky, Melting of interference in the fractional quantum Hall effect: Appearance of neutral modes, Phys. Rev. Lett. **122**, 246801 (2019).

[39] V. Venkatachalam, S. Hart, L. Pfeiffer, K. West, and A. Yacoby, Local thermometry of neutral modes on the quantum Hall edge, Nat. Phys. **8**, 676 (2012).

[40] M. Banerjee, M. Heiblum, V. Umansky, D. E. Feldman, Y. Oreg, and A. Stern, Observation of half-integer thermal Hall conductance, Nature (London) **559**, 205 (2018).

[41] M. Banerjee, M. Heiblum, A. Rosenblatt, Y. Oreg, D. E. Feldman, A. Stern, and V. Umansky, Observed quantization of anyonic heat flow, Nature (London) **545**, 75 (2017).

[42] R. A. Melcer, A. Gil, A. K. Paul, P. Tiwari, V. Umansky, M. Heiblum, Y. Oreg, A. Stern, and E. Berg, Heat conductance of the quantum Hall bulk, Nature (London) **625**, 489 (2024).

[43] J. Hayakawa, K. Muraki, and G. Yusa, Real-space imaging of fractional quantum Hall liquids, Nat. Nanotechnol. **8**, 31 (2013).

[44] A. Kamiyama, M. Matsuura, J. N. Moore, T. Mano, N. Shibata, and G. Yusa, Real-time and space visualization of excitations of the $\nu = 1/3$ fractional quantum Hall edge, Phys. Rev. Res. **4**, L012040 (2022).

[45] A. Kamiyama, M. Matsuura, J. N. Moore, T. Mano, N. Shibata, and G. Yusa, Dynamics of the fractional quantum Hall edge probed by stroboscope measurements of trions, Appl. Phys. Lett. **122**, 202103 (2023).

[46] Q. France, Y. Jeong, A. Kamiyama, T. Mano, K. ichi Sasaki, M. Hotta, and G. Yusa, Electrically induced bulk and edge excitations in the fractional quantum Hall regime, Phys. Rev. Lett. **135**, 066203 (2025).

[47] Z.-X. Hu, X. Wan, and P. Schmitteckert, Trapping Abelian anyons in fractional quantum Hall droplets, Phys. Rev. B **77**, 075331 (2008).

[48] Z. Papić, R. S. K. Mong, A. Yazdani, and M. P. Zaletel, Imaging anyons with scanning tunneling microscopy, Phys. Rev. X **8**, 011037 (2018).

[49] S. Pu, A. C. Balram, Y. Hu, Y.-C. Tsui, M. He, N. Regnault, M. P. Zaletel, A. Yazdani, and Z. Papić, Fingerprints of composite fermion Lambda levels in scanning tunneling microscopy, Phys. Rev. B **110**, L081107 (2024).

[50] M. Gattu, G. J. Sreejith, and J. K. Jain, Scanning tunneling microscopy of fractional quantum Hall states: Spectroscopy of composite-fermion bound states, Phys. Rev. B **109**, L201123 (2024).

[51] Y. Hu, Y.-C. Tsui, M. He, U. Kamber, T. Wang, A. S. Mohammadi, K. Watanabe, T. Taniguchi, Z. Papić, M. P. Zaletel, and A. Yazdani, High-resolution tunnelling spectroscopy of fractional quantum Hall states, Nat. Phys. **21**, 716 (2025).

[52] F. D. M. Haldane, Fractional quantization of the Hall effect: A hierarchy of incompressible quantum fluid states, Phys. Rev. Lett. **51**, 605 (1983).

[53] Y. Park and F. D. M. Haldane, Guiding-center Hall viscosity and intrinsic dipole moment along edges of incompressible fractional quantum Hall fluids, Phys. Rev. B **90**, 045123 (2014).

[54] Y. Yang and Z.-X. Hu, Monte Carlo simulation of the topological quantities in fractional quantum Hall systems, Phys. Rev. B **107**, 115162 (2023).

[55] W.-Q. Yang, Q. Li, L.-P. Yang, and Z.-X. Hu, Neutral excitation and bulk gap of fractional quantum Hall liquids in disk geometry, Chin. Phys. B **28**, 067303 (2019).

[56] Y. Yang, S. Pu, Y. Hu, and Z.-X. Hu, Simulating composite fermion excitons on a disk by density functional theory and Monte Carlo, Phys. Rev. B **111**, 195139 (2025).

[57] Y.-L. Wu, B. Estienne, N. Regnault, and B. A. Bernevig, Braiding non-Abelian quasiholes in fractional quantum Hall states, Phys. Rev. Lett. **113**, 116801 (2014).

[58] Q. Li, N. Jiang, Z. Zhu, and Z.-X. Hu, The length scale measurements of the fractional quantum Hall state on a cylinder, New J. Phys. **17**, 095006 (2015).

[59] Z. Liu, R. N. Bhatt, and N. Regnault, Characterization of quasiholes in fractional Chern insulators, Phys. Rev. B **91**, 045126 (2015).

[60] J. Li, D. Ye, C.-X. Jiang, N. Jiang, X. Wan, and Z.-X. Hu, Anyonic braiding via quench dynamics in fractional quantum Hall liquids, Phys. Rev. B **105**, 195311 (2022).

[61] https://github.com/zxhucqu/DynamicsFQH.

[62] S. Johri, Z. Papić, R. N. Bhatt, and P. Schmitteckert, Quasiholes of $\frac{1}{3}$ and $\frac{7}{3}$ quantum Hall states: Size estimates via exact diagonalization and density-matrix renormalization group, Phys. Rev. B **89**, 115124 (2014).